4-2016

Utilizing tunable signal interference control topologies with electromechanical resonators

Bryce A. Geesey
Purdue University

Graduate School Form
30 Updated 12/26/2015

PURDUE UNIVERSITY
GRADUATE SCHOOL
Thesis/Dissertation Acceptance

This is to certify that the thesis/dissertation prepared

By Bryce A. Geesey

Entitled

UTILIZING TUNABLE SIGNAL INTERFERENCE CONTROL TOPOLOGIES WITH ELECTROMECHANICAL RESONATORS

For the degree of Master of Science in Mechanical Engineering

Is approved by the final examining committee:

Dr. Jeffrey F. Rhoads
Chair

Dr. Charles M. Krousgrill

Dr. George T.-C. Chiu

To the best of my knowledge and as understood by the student in the Thesis/Dissertation Agreement, Publication Delay, and Certification Disclaimer (Graduate School Form 32), this thesis/dissertation adheres to the provisions of Purdue University's "Policy of Integrity in Research" and the use of copyright material.

Approved by Major Professor(s): Dr. Jeffrey F. Rhoads

Approved by: Dr. Jay P. Gore 4/19/2016

Head of the Departmental Graduate Program Date

UTILIZING TUNABLE SIGNAL INTERFERENCE CONTROL TOPOLOGIES WITH ELECTROMECHANICAL RESONATORS

A Thesis

Submitted to the Faculty

of

Purdue University

by

Bryce A. Geesey

In Partial Fulfillment of the

Requirements for the Degree

of

Master of Science in Mechanical Engineering

May 2016

Purdue University

West Lafayette, Indiana

ACKNOWLEDGMENTS

I would like to thank my advisor, Dr. Jeff Rhoads, for inspiring me to pursue a graduate degree in engineering and for his guidance in completing this work. Thank you also to Nikhil Bajaj for his support and advice towards building the experimental electronic circuits in this work.

This thesis is based in part upon work supported by the National Science Foundation under grant numbers 1233780 and 1247893. Any opinions, findings, and conclusions or recommendations expressed in this document are those of the author and do not necessarily reflect the views of the National Science Foundation.

TABLE OF CONTENTS

LIST OF TABLES

LIST OF FIGURES

Figure Page

Figure Page

ABSTRACT

Geesey, Bryce A. M.S.M.E., Purdue University, May 2016. Utilizing Tunable Signal Interference Control Topologies with Electromechanical Resonators. Major Professor: Jeffrey F. Rhoads, School of Mechanical Engineering.

Exploiting knowledge gained from previous investigations of channelized and transversal filters, signal interference filters use transmission line differences to generate transmission zeros through phase-shifted combinations of signals at the output of a device. The transmission lines used in these circuits are straightforward to design, but are limited to high-frequency signals (on the order of a few gigahertz) due to the necessity for spatial compactness and low loss. More recent studies have used electromechanical resonators to achieve phase shifting and quality factor improvements at slightly-lower frequencies. These concepts may prove useful if extended to micro- and nanoscale resonators.

To explore signal interference topologies outside of purely-electrical, high-frequency filtering domains, a generic system model is proposed herein, which is based upon high quality factor resonant elements and continuously-tunable amplitude and phase components. The mathematical models developed in this work are generalized to apply the concept of signal interference to a variety of linear resonant systems. With this approach, frequency response behaviors can be quickly modified from amplification to cancellation through appropriate tuning of the phase and gain components.

The analytical models are simulated and implemented in electromechanical circuitry as a first step towards system integration. The prototypical circuits qualitatively match the desired frequency response and tuning behaviors, proving the use of the mathematical models in the design of linear resonant signal interference systems.

CHAPTER 1. INTRODUCTION

1.1 Background

Resonant micro- and nanoelectromechanical systems (M/NEMS) have been actively studied over the past few decades due to their potential to respond within nanoseconds to changing inputs and provide observable resonance behaviors up to microwave frequencies. The high quality (Q) factors of these devices enable narrow-band selectivity and improved signal-to-noise strength compared to their purely-electrical analogues. These systems can also exhibit unique and useful nonlinearities, which has further encouraged and facilitated the application of M/NEMS resonators in, for example, mass and magnetic field sensing, signal amplification and filtering, and timing circuits [1]. Another important attribute of M/NEMS is their inherently small size, which motivates modeling these devices for very-large-scale integration (VLSI) [2].

Recently, signal interference architectures have been proposed for low-loss, purely-electrical filtering circuits. These devices create destructive interference (transmission zeros) through phase-shifted output combinations [3–7]. Signal interference filters arose as passive adaptations of the active transversal or channelized filter concepts primarily investigated by Rauscher [8, 9], which is why signal interference filters are often referred to as transversal filtering sections (TFS). The basic operating principle of both transversal active filters and signal interference filters is in the output summation of two or more signal paths originating from a single source. By individually altering the amplitude and phase characteristics of each signal path, the recombined output responses demonstrate constructive interferences at frequencies where the signals are collectively in-phase and destructive interferences where the signal phases are opposed.

These multi-path filtering topologies have also been implemented with tunable concepts based upon, for example, transmission line switching and varactor diodes [10, 11] or reconfigurable coupling [12] for passive filters, and varactor tuning for active channelized filters [13]. The passive studies claim to achieve transitions from narrow-band band-pass filters to wide-band ones (at gigahertz frequencies) through appropriate switching and tuning elements [11]. Transversal interference architectures have therefore been demonstrated in a number of electrical signal filtering contexts with a reasonable degree of success, suggesting that this simple concept could prove useful in other domains.

The aforementioned studies of electromechanical and purely-electrical systems focus on shaping the near-resonant frequency response of the devices. Broadly speaking, interference filters accomplish frequency shaping in a static sense through transmission line differences in TFSs, whereas electromechanical techniques can leverage linear Lorentzian responses or inherently nonlinear dynamics (e.g. Duffing-like structures) in the frequency domain [1, 2, 14–16]. MEMS oscillators and timing circuits achieve frequency response stability and noise reduction with closed-loop *feedback* phase shifting [17, 18]. In an effort to easily amplify or cancel frequency domain behaviors, this work investigates tuning the resonant frequency response of high-Q mechanical devices using the *feedforward* properties of signal interference. The proposed dynamic control systems exhibit a wide range of resonance and cancellation behaviors through the simple tuning of signal interference components. Generalized mathematical models are developed here, which are then simulated and implemented in analog circuitry as a step towards other domains and implementations, including M/NEMS.

1.2 Project Goals

This work studies signal interference concepts outside of purely-electrical filtering contexts to leverage their benefits of spatial compactness and simplicity in resonant mechanical systems. Additionally, a parametrically-tunable system model is desired

to further adapt signal interference to a wider range of problems by removing domain-specific constraints on frequency, amplitude, and phase. To accomplish these goals, the work presented here is organized in two main parts. First, dynamic system models are developed for the proposed transversal feedforward system architectures. These first-principles based models are generalized in a dimensionless sense to be applied to a variety of resonant physical systems. Second, simulated and experimental proof-of-concept devices are developed to show the applicability of the mathematical model to a simple physical system. The experimental setups also prove the utility of the model and an associated set of design equations for resonant signal interference systems.

1.3 Technical Approach

In the context of signal interference filters, simple passive transmission lines may be used to alter the amplitude and phase characteristics of individual signal channels before recombining them at an output. This works well in electrical filters at gigahertz frequencies, where the necessary path-length differences required to generate appreciable phase offsets are short due to the small wavelengths involved. For a more generic signal interference system that can model any arbitrary frequency range, a more robust construction must be utilized.

Recent investigations of signal interference filters have incorporated the resonance-amplification and phase-shifting benefits of electromechanical resonators in the signal paths [7, 19]. The high-Q characteristics of these resonators aid the filtering effect at lower frequencies and provide an additional phase shift of about $-90°$ near resonance. However, the surface acoustic wave (SAW) resonators used in these studies included several spurious modes due to their geometry and manufacturing tolerances, which negatively impact the output responses of the filters. Figure 1.1 shows simplified diagrams of (a) transmission line signal interference filters and (b) signal interference filters including electromechanical resonators and transmission lines.

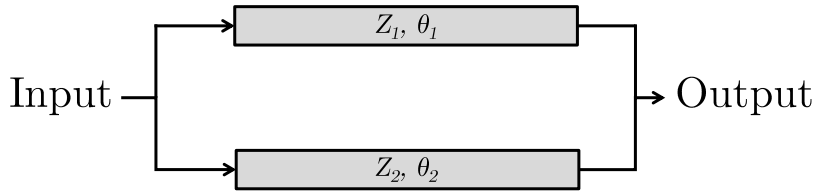

(a)

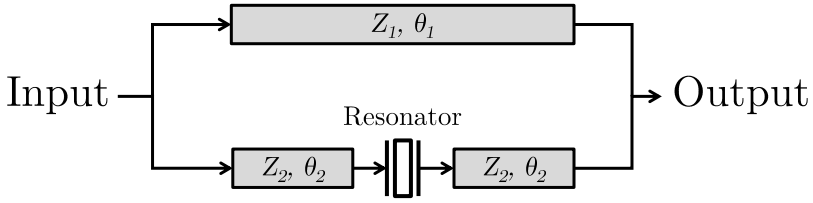

(b)

Figure 1.1. Typical block diagrams of signal interference filters consisting of (a) solely transmission line amplitude differences (Z_1 and Z_2) and path-length differences (θ_1 and θ_2) and (b) a combination of transmission lines and an electromechanical resonator.

The dynamic models developed in this work incorporate ideal Lorentzian resonant elements along with ideal gain and phase-shifting components. By starting with an ambiguous and idealized model system, it is assumed that the equations and results obtained in the following chapters may be appropriately related to a diverse set of physical structures and processes.

CHAPTER 2. RESONANT SIGNAL INTERFERENCE SYSTEM MODELS

To better understand the signal-interference-type system in a linear sense, first-principles models are developed here from an understanding of Lorentzian frequency behaviors of electromechanical systems. The first approach starts with a single resonant element with a separate feedforward interference structure. This control setup demonstrates some of the results that have been achieved in prior signal interference systems based on surface acoustic wave (SAW) resonators [7,19], but in a non-domain-specific sense. The second approach then extends the model to include a second resonant element, independent of the first, inside the feed-forward interference structure. This topology demonstrates the myriad of frequency response shapes that are possible by simple combinations of tunable linear resonances. This chapter concludes with a discussion of the assumptions and limitations included in these signal interference system models.

2.1 Resonator Equation of Motion

Classical linear motion of a mechanical resonator is utilized as a starting point from which to evaluate the behavior of the resonant elements in a given signal interference system. The equation of motion adopted here is then generalized through a process called non-dimensionalization, which seeks to remove all dimensions from a problem to observe its solutions independent of the domain, process, or environment. Normalizing systems in this way is common and useful in differential equation models since it can parameterize a problem to fit multiple scenarios.

First, the resonator is modeled by the classic inhomogeneous, second-order, linear differential equation of motion:

$$m\ddot{x} + c\dot{x} + kx = F\sin(\omega t) \tag{2.1}$$

where m, c, and k are the effective mass, damping, and stiffness parameters associated with the resonator (assumed to be constants), t is the time variable, and x is the desired resonator output. The right hand side of Equation (2.1), $F\sin(\omega t)$, is a sinusoidal forcing input with amplitude F and angular frequency ω. This equation of motion is scaled by dividing by m and then non-dimensionalized using the following definitions:

$$\begin{aligned} x &= x_0\hat{x} & \omega t &= r\tau \\ r &= \frac{\omega}{\omega_n} & \omega_n &= \sqrt{\frac{k}{m}} \\ 2\zeta &= \frac{c}{\sqrt{mk}} & (\bullet)' &= \frac{d(\bullet)}{d\tau} \\ x_0 &= \frac{F}{k} \end{aligned} \tag{2.2}$$

where x_0 is an arbitrary scaling parameter of x such that $\hat{x}$ is non-dimensional, ζ is the canonical damping ratio, ω_n is the undamped natural frequency of the resonator, and r and τ are normalized frequency and time variables, respectively. The arbitrary definition $x_0 = F/k$ allows the dependence on input amplitude (F) and resonator stiffness (k) to be completely removed from this model. Since the $\dot{(\bullet)}$ operator in Equation (2.1) represents a derivative with respect to time t, the substitution of τ for t requires the definition of the new derivative operator $(\bullet)'$ with respect to τ. It is also important to note that the quality factor Q of the resonator can be defined with respect to the dimensionless damping ratio ζ as $Q = 1/2\zeta$. Performing all of the above substitutions gives the form:

$$\hat{x}'' + 2\zeta\hat{x}' + \hat{x} = \sin(r\tau) \tag{2.3}$$

The solution to this simplified differential equation involves independent homogeneous and particular components. The transient behavior (homogeneous solution) of this system is ignored here since steady-state effects are the more useful results of signal interference systems, and transient behavior cannot be easily generalized since it depends on specific initial conditions. Therefore, only the particular solution is pursued here, assuming transient effects are allowed to decay during system initialization. Using the method of undetermined coefficients, the particular solution of Equation (2.3) is:

$$\begin{aligned} \hat{x}_p(\tau) &= \hat{A}\sin(r\tau) + \hat{B}\cos(r\tau) \\ \hat{A} &= \frac{-(r^2-1)}{\sqrt{(r^2-1)^2+(2\zeta r)^2}} \\ \hat{B} &= \frac{-2\zeta r}{\sqrt{(r^2-1)^2+(2\zeta r)^2}} \end{aligned} \tag{2.4}$$

This form of the particular solution is more difficult to evaluate since it includes two separate magnitude terms and both sine and cosine components. Equation (2.4) can be condensed through trigonometric identities using the definitions $\hat{C} = \sqrt{\hat{A}^2 + \hat{B}^2}$ and $\tan\psi = \hat{B}/\hat{A}$ to combine the two terms into one. Doing this modifies the particular solution to:

$$\begin{aligned} \hat{x}_p(\tau) &= \hat{C}\sin(r\tau + \psi) \\ \hat{C} &= \frac{1}{\sqrt{(r^2-1)^2+(2\zeta r)^2}} \\ \psi &= \arctan\left(\frac{2\zeta r}{r^2-1}\right) \end{aligned} \tag{2.5}$$

which is straightforward to evaluate in the frequency domain as the amplitude $\hat{C}$ and phase ψ responses of the equation of motion. Now that the resonant response is well defined, the signal interference structure can be added around this solution.

2.2 Single Resonator Signal Interference System

The proposed single resonator control design consists of a source signal that is split into two signal paths, one that passes through a simple resonator and another that passes through an ideal phase shifter ϕ and amplifier G, which are then added together at the output. A model of this system is shown in Figure 2.1.

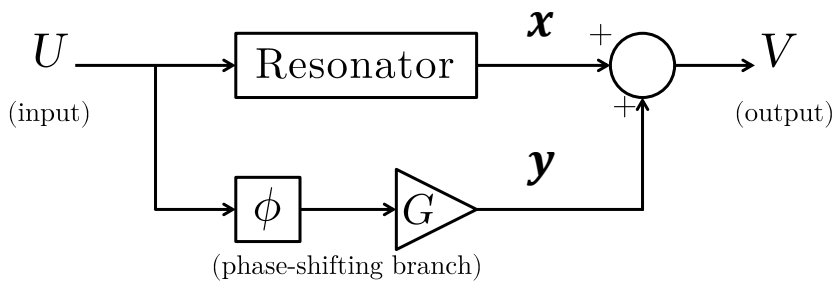

Figure 2.1. Block diagram of the proposed control system with two signal branches, one with a resonator and another with a pure phase-shifter ϕ and gain G. The input U is split equally between the two branches, and the output V is the non-weighted sum of the individual responses x and y.

This system is evaluated by supplying the sinusoidal input $U = F\sin(\omega t)$ described above to determine the steady-state output V. To calculate the output in this configuration, the resonator response x from the previous section is added to the phase-shifted signal y. The phase-shifted branch y has a response of the form:

$$y = GF\sin(\omega t + \phi) \tag{2.6}$$

where the phase ϕ is assumed to add linearly to the argument of the input sinusoid, and the amplitude G is assumed to scale the input linearly. To sum the responses of x and y and maintain the desired level of generality, the y signal branch must also be put in a non-dimensional form using a similar scheme as above. Here, the definition $y_0 = x_0 = F/k$ is incorporated for dimensional similarity between the two signal paths, and these substitutions give the form:

$$\hat{y} = Gk\sin(r\tau + \phi) \tag{2.7}$$

Combining Equation (2.5) and Equation (2.7), the non-dimensional output $\hat{V}$ of the system can be determined:

$$\begin{aligned} \hat{V} &= \hat{x}_p(\tau) + \hat{y}(\tau) \\ \hat{V} &= \hat{C}\sin(r\tau + \psi) + Gk\sin(r\tau + \phi) \end{aligned} \tag{2.8}$$

As mentioned in the previous section, this steady-state form of the output solution is more difficult to evaluate with two amplitude terms and two phase components, so a single-term combined result is desired. The trigonometric sum of angles identity was used here on each sine term to yield:

$$\begin{aligned} \hat{V} = \hat{C}[&\sin(r\tau)\cos\psi + \cos(r\tau)\sin\psi] \\ &+ Gk[\sin(r\tau)\cos\phi + \cos(r\tau)\sin\phi] \end{aligned} \tag{2.9}$$

Collecting terms, this simplifies to:

$$\begin{aligned} \hat{V} = [&\hat{C}\cos\psi + Gk\cos\phi]\sin(r\tau) \\ &+ [\hat{C}\sin\psi + Gk\sin\phi]\cos(r\tau) \end{aligned} \tag{2.10}$$

This can be combined into a single sine term with definitions of $\hat{D}$ and θ:

$$\begin{aligned} \hat{D} &= \sqrt{[\hat{C}\cos\psi + Gk\cos\phi]^2 + [\hat{C}\sin\psi + Gk\sin\phi]^2} \\ \tan\theta &= \frac{\hat{C}\sin\psi + Gk\sin\phi}{\hat{C}\cos\psi + Gk\cos\phi} \end{aligned} \tag{2.11}$$

giving the final non-dimensional form:

$$\begin{aligned} \hat{V} &= \hat{D}\sin(r\tau + \theta) \\ \hat{D} &= \sqrt{\hat{C}^2 + (Gk)^2 + 2\hat{C}Gk\cos(\psi - \phi)} \\ \theta &= \arctan\left(\frac{\sin\psi + \frac{Gk}{\hat{C}}\sin\phi}{\cos\psi + \frac{Gk}{\hat{C}}\cos\phi}\right) \end{aligned} \tag{2.12}$$

The magnitude ($\hat{D}$) of the output in Equation (2.12) depends on four parameters. First, the $\hat{C}$ term is a non-dimensional gain that exhibits a resonant behavior with respect to the normalized frequency r, tending to $1/2\zeta$ (the quality factor, Q) when $r = 1$ [see Equation (2.5)]. Second, the product Gk is the non-dimensional constant gain of the phase-shifted branch. Third, the angle ψ is the phase of the resonator, which is 0° far below the resonant frequency and -180° far above resonance. Defining the resonant frequency as $\omega_r = \omega_n\sqrt{1-2\zeta^2}$, or $r_r = \omega_r/\omega_n = \sqrt{1-2\zeta^2}$, means that ψ depends on ζ near resonance, according to Equation (2.5), and ψ is approximately -90° at resonance for a high quality factor (low ζ) device. Lastly, the design parameter ϕ is a constant and tunable phase that can change the argument of the cosine term, altering the qualitative behavior of the system.

To better understand how ϕ affects the frequency response of the system, Equation (2.12) can be further evaluated at the resonant frequency $r_r = \omega_r/\omega_n = \sqrt{1-2\zeta^2}$, which yields the resonance relationship:

$$\begin{aligned}
\hat{V} &= \hat{D}\sin\left(\tau\sqrt{1-2\zeta^2}+\theta\right) \\
\hat{D} &= \sqrt{\frac{1}{(2\zeta^2)(1-\zeta^2)} + (Gk)^2 + \frac{Gk}{\zeta\sqrt{1-\zeta^2}}\cos(\psi-\phi)} \\
\theta &= \arctan\left(\frac{\sin\psi + 2\zeta\sqrt{1-\zeta^2}Gk\sin\phi}{\cos\psi + 2\zeta\sqrt{1-\zeta^2}Gk\cos\phi}\right)
\end{aligned} \tag{2.13}$$

Clearly, the output amplitude $\hat{D}$ at resonance is fixed for a given constant ζ and k except for the design variables ϕ and G. Varying ϕ adjusts the resonant amplitude from a maximum at $\phi = -90^\circ$ (ϕ is in-phase with ψ) to a minimum at $\phi = 90^\circ$ (ϕ is 180° out-of-phase from ψ). In Equation (2.13), this behavior is due to the cosine function reaching a maximum when its argument is 0° and a minimum when the argument is $+/-180^\circ$. If the gain is matched between the two signal branches by the definition $Gk = 1/(2\zeta\sqrt{1-\zeta^2})$, the minimum resonant amplitude is zero.

Figure 2.2 shows the described behavior of the resonant amplitude for this assigned definition of Gk and values of ϕ from -180° to 180°. This phenomenon is

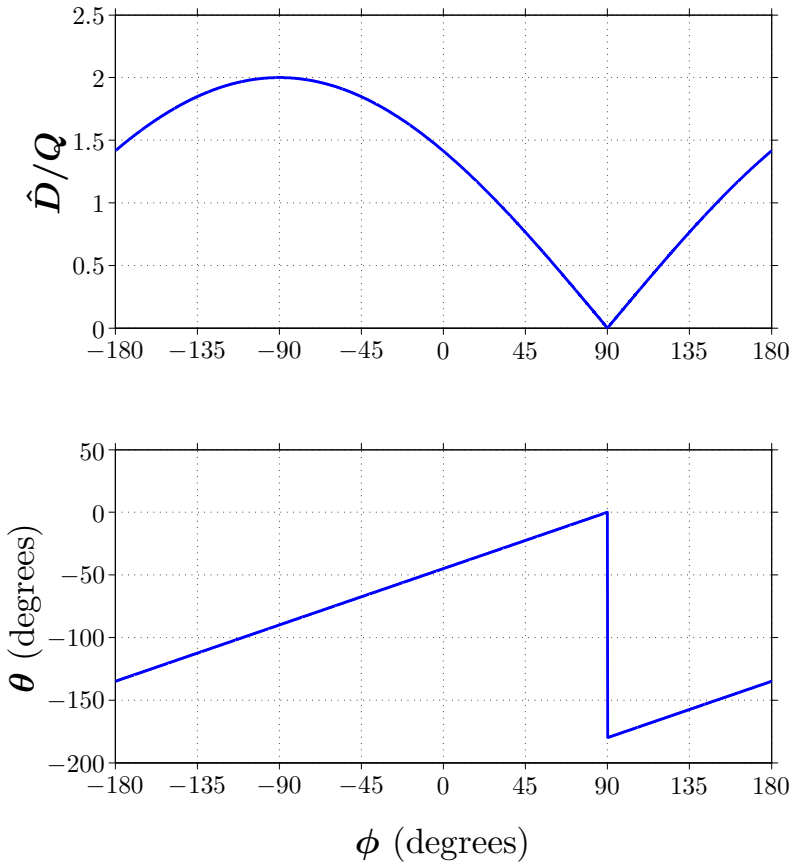

Figure 2.2. Theoretical phase θ and Q-scaled amplitude $\hat{D}$ of the non-dimensional output $\hat{V}$, evaluated at resonance ($r = \omega_r/\omega_n = \sqrt{1-2\zeta^2}$), plotted with respect to the tunable design parameter ϕ. At $\phi = -90°$ the resonant amplitude is doubled, and at $\phi = 90°$ the amplitude is canceled.

the operating principle of signal-interference-type circuits in which two signals create transmission zeros where their phases are exactly 180° opposed, and they create doubled amplitudes where their phases are the same, also described as destructive and constructive interference, respectively.

With this understanding of resonance behavior, the frequency of the input is swept near resonance [in Equation (2.12)] for a few characteristic values of ϕ. The pattern of the response curves is shown in Figure 2.3, assuming a nominally high value of 10,000

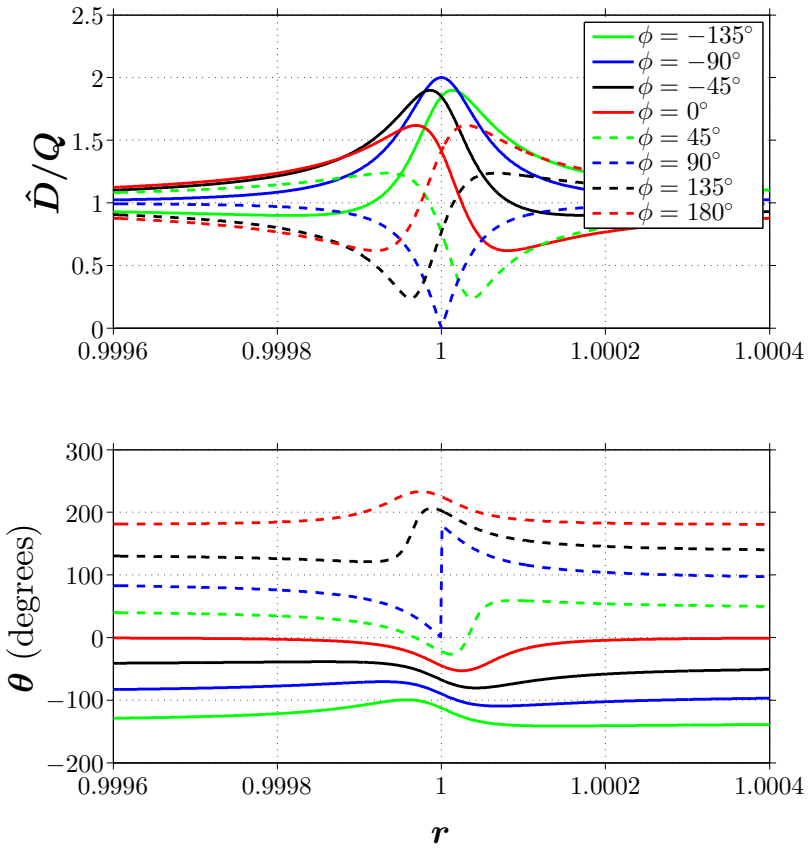

Figure 2.3. Various theoretical frequency responses of the non-dimensional system output $\hat{V}$ at frequencies r in a small range near $r = 1$ for characteristic values of ϕ at 45° intervals. Clearly, $\phi = -90°$ and $\phi = 90°$ lead to constructive and destructive interference, respectively. Other values of ϕ map the transitions between the two extremes. Resonance occurs in a narrow range of frequencies near $r = 1$ due to the high-Q assumption, with Q nominally set to 10,000 here.

for Q to determine the phase and frequency scales. The amplitude response also depends on Q, where the height of the resonant peak is determined by the inherent damping of the resonator. As in Figure 2.2, the amplitude plot here is scaled by Q to show the amplitude doubles for $\phi = -90°$ with respect to any arbitrarily-high Q value.

The qualitative potential of the proposed system is visible in the response of Figure 2.3, namely the amplification or cancellation of a specific input frequency that results from appropriate tuning of the phase-shift design parameter ϕ. A variety of literature already exists describing the amplification and cancellation behaviors of electrical filtering as observed here, however the continuously-tunable control system designed above shows useful characteristics from which a variety of suitable physical analogues may be derived.

2.3 Two Resonator Signal Interference System

Using the same method as above, the control topology of Figure 2.1 may be extended to include a resonator in the phase-shifting branch as well. This setup is shown in Figure 2.4, where y now represents the response of the second resonator and z is the output of the second branch after phase shifting (ϕ) and amplifying (G).

Since the first signal branch here is unchanged from the single resonator case, the equation of motion and its non-dimensionalized form are the same as those presented in Equations (2.1) and (2.3) with the addition of subscripts on the damping ratio (ζ_1), natural frequency (ω_{n1}), and other resonator parameters to denote the first resonator. Thus, the particular solution of the first resonator equation of motion is again:

$$\begin{aligned} \hat{x}_p(\tau) &= \hat{C}_1 \sin(r\tau + \psi_1) \\ \hat{C}_1 &= \frac{1}{\sqrt{(r^2-1)^2 + (2\zeta_1 r)^2}} \\ \psi_1 &= \arctan\left(\frac{2\zeta_1 r}{r^2-1}\right) \end{aligned} \tag{2.14}$$

To evaluate the other signal branch, the second resonator is modeled independently with a similar second-order differential equation:

$$m_2\ddot{y} + c_2\dot{y} + k_2 y = U = F\sin(\omega t) \tag{2.15}$$

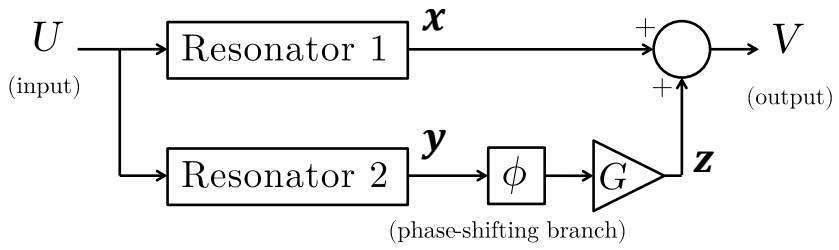

Figure 2.4. Block diagram of the proposed two resonator control system where each signal branch contains a resonator, and the second branch also includes a pure phase-shifter ϕ and gain G. The input U is split equally between the two branches, y is the response of the second resonator, and the output V is the non-weighted sum of the individual branch responses x and z.

This form was non-dimensionalized using the same approach as Equation (2.2), which also introduces ω_{n1} into the equation of motion for the second resonator to maintain dimensional similarity between signal branches. This is simplified with the definitions:

$$\begin{aligned} 2\zeta_2 &= \frac{c_2}{\sqrt{m_2 k_2}} & \omega_{n2} &= \sqrt{\frac{k_2}{m_2}} \\ y_0 &= \frac{F}{k_2} & \alpha &= \frac{\omega_{n2}}{\omega_{n1}} \end{aligned} \tag{2.16}$$

where α is a detuning parameter for the natural frequencies of the two resonators. The non-dimensional frequency parameter r is still defined here as $r = \omega/\omega_{n1}$. The second resonator equation of motion is now:

$$\hat{y}'' + 2\zeta_2 \alpha \hat{y}' + \alpha^2 \hat{y} = \alpha^2 \sin(r\tau) \tag{2.17}$$

Again, using the method of undetermined coefficients, the particular solution of this equation is given by:

$$\begin{aligned}\hat{y}_p(\tau) &= \hat{C}_2 \sin(r\tau + \psi_2) \\ \hat{C}_2 &= \frac{\alpha^2}{\sqrt{(r^2-\alpha^2)^2 + (2\zeta_2\alpha r)^2}} \\ \psi_2 &= \arctan\left(\frac{2\zeta_2\alpha r}{r^2-\alpha^2}\right)\end{aligned} \tag{2.18}$$

Next, the ideal phase shift and gain blocks are applied to the $\hat{y}_p$ response, which yields:

$$\hat{z}(\tau) = G\hat{C}_2 \sin(r\tau + \psi_2 + \phi) \tag{2.19}$$

The $\hat{z}$ response is then summed with $\hat{x}_p$ and simplified using trigonometric identities to obtain the final form of the output:

$$\begin{aligned}\hat{V} &= \hat{D} \sin(r\tau + \theta) \\ \hat{D} &= \sqrt{\hat{C}_1^2 + G^2\hat{C}_2^2 + 2G\hat{C}_1\hat{C}_2 \cos(\psi_1 - \psi_2 - \phi)} \\ \theta &= \arctan\left(\frac{\hat{C}_1 \sin(\psi_1) + G\hat{C}_2 \sin(\psi_2 + \phi)}{\hat{C}_1 \cos(\psi_1) + G\hat{C}_2 \cos(\psi_2 + \phi)}\right)\end{aligned} \tag{2.20}$$

In the single resonator system, there were two design variables to tune the output interference response, ϕ and G, for a given high-Q resonator. Now in the two resonator system there are three design variables to tune, ϕ, G, and α, assuming that the two resonators have the same high-Q value. The frequency response space can be mapped by adjusting these three parameters independently. Figure 2.5 shows various amplitude response shapes that can be obtained by setting $G = 1$ and adjusting ϕ and α for a pair of resonators with $Q = 10,000$. The ϕ parameter is iterated from 0° to 180° in 45° intervals, and α is adjusted slightly above and below unity corresponding to natural frequency differences of 1 and 1.5 times the resonators' bandwidth.

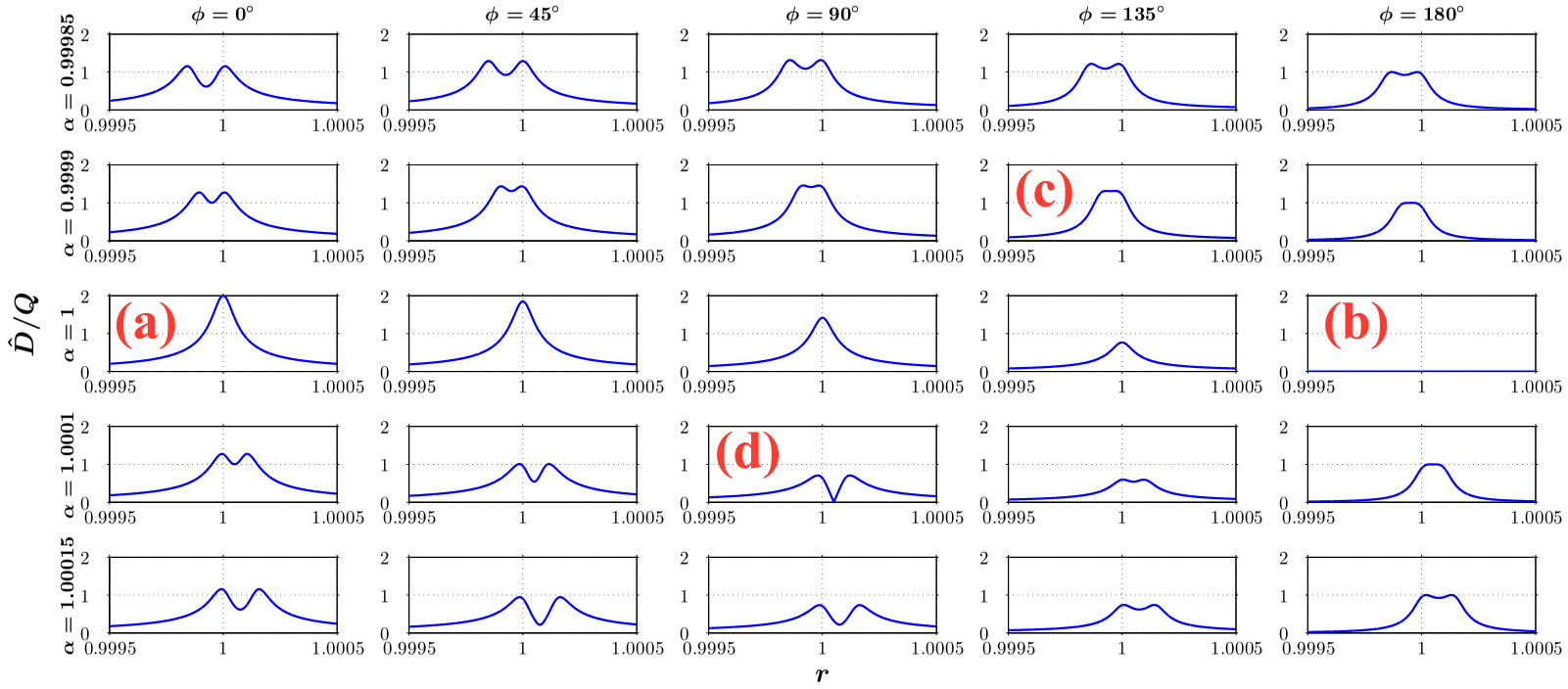

Figure 2.5. Various theoretical frequency responses of the two resonator system output amplitude $\hat{D}$ scaled by the resonators' Q factor of 10,000. Here, G is chosen to be unity, while ϕ is iterated from 0° to 180° and the frequency detuning parameter α is adjusted slightly above and below unity. The horizontal axis is the normalized frequency r in a narrow range near $r = 1$. These results show (a) amplitude doubling, (b) complete amplitude cancellation, (c) band-pass-type responses, (d) combinations of resonance and cancellation.

The results of Figure 2.5 show (a) amplitude doubling at resonance where the resonators are in-phase ($\phi = 0°$) and have the same natural frequency ($\alpha = 1$), (b) complete amplitude cancellation ($\phi = 180°$ and $\alpha = 1$), (c) a flat band-pass-type response, (d) combinations of resonance and cancellation, etc. Results (a) and (b) are intuitively referred to as constructive and destructive interferences, respectively, making results such as (c) and (d) the more unusual and interesting ones to replicate experimentally. According to Yagubizade [20], a band-pass-type response obtained from the output of two parallel resonators is optimally flat when the resonators' natural frequencies are offset by one bandwidth, as in (c).

As with the single resonator case, the qualitative potential of this proposed topology is in shaping the frequency behavior of a system by simply combining two independent linear resonance responses. The theoretical results of this study may now be employed in a physical proof-of-concept.

2.4 Model Limitations

To develop the system models presented in this chapter, a number of simplifying assumptions were made. The homogeneous solution to the resonator equation of motion was ignored because transient responses based on initial conditions quickly decay in many second-order linear systems. This assumption imposes a steady-state condition on the responses for which these models are appropriate; i.e. the system must be allowed to oscillate for long enough that transient effects are no longer significant. In physical experiments this may simply mean allowing sufficient settling time when changing the frequency or amplitude of the forcing input.

Additionally, it was discovered that the single resonator signal interference systems impose a gain definition of $Gk = 1/(2\zeta\sqrt{1-\zeta^2})$ to obtain a complete destructive interference (transmission zero) at resonance when $\phi = 90°$. In the two resonator system, this corresponds to a definition of $G = 1$ to match the resonant amplitudes of each signal path. The two resonator system also requires knowing the quality

factors of the resonators so the α detuning parameter may be adequately set based on the bandwidths. In these models it was assumed that both resonators have the same quality factor, but this may not be the case depending on the specific physical implementation or manufacturing tolerances.

Linear resonance is considered in this work and it is assumed the resonators are not coupled, however nonlinear effects are commonly encountered in M/NEMS and other physical systems. This work may be expanded in the future to account for familiar nonlinearities, such as Duffing responses, or inter-resonator coupling. Similarly, it is assumed that the ideal phase and gain elements are linear and constant in the frequency domain, although physical implementations of these elements may be frequency dependent.

CHAPTER 3. PROTOTYPE DESIGN AND SIMULATION

3.1 Developing a Prototype System in Electromechanical Circuits

As previously stated, the goal of this work is to study signal interference concepts outside of the purely-electrical filtering domain. To validate the mathematical results described above, any linear resonant system may be used, but an electromechanical circuit is prescribed in this chapter due to the commercial availability and rapid assembly and test benefits of electronics. Mechanical, acoustic, optical, magnetic, and biological resonant systems, for example, may be amenable to this signal interference approach, however they typically incur higher manufacturing time and cost and may be more difficult to observe compared to commercial electromechanical components.

3.1.1 Frequency Considerations

Signal interference circuits have been demonstrated in wireless frequency ranges from several hundred megahertz to a few gigahertz using passive setups [5, 19]. However, MEMS and NEMS resonators can operate at much lower frequencies (for example, around 42.7 kHz in a MEMS [21] and 25 MHz in a NEMS [2, 22]). At lower frequency ranges the required electrical lengths of the passive transmission line elements in signal interference devices become too significant for practical use with small systems. An active circuit was derived here instead of a passive one due to this limitation and to prove the modeled results can be scaled to lower frequency ranges than prior work.

In this work, simulations and experimental implementations of the control systems of Figures 2.1 and 2.4 are proof-of-concept architectures at a nominal resonator frequency of 50 MHz. A 50 MHz nominal frequency is chosen to demonstrate a lower frequency application than previous signal interference devices while also being suf-

ficiently fast to accommodate some state-of-the-art M/NEMS capabilities. In theory and practice the resonator may be any high-Q system accurately modeled by Equation (2.3).

In an electromechanical system, it may at first seem advantageous to observe the input and resonator output in order to process the phase-shifting, gain, and summation steps in a digital implementation. However, sampling at 10 times the input frequency means a sample-and-hold operation results in a phase lag of 36° between samples, and sampling at 100 times the input frequency still yields 3.6° of lag. For less than 1° of phase error, the sampling rate of a digital implementation must be at least 360 times the input frequency, which becomes impractical at a nominal resonator frequency of 50 MHz. A digital implementation also involves discrete-time operations, which reduce the applicability to continuous-time systems. For these reasons, an analog signal processing chain was selected.

3.1.2 Resonator Design

A piezoelectric crystal resonator was selected for this proof-of-concept system. Piezoelectric devices are readily available, well understood, and cost-effective. They are also commonly used in oscillators and timing circuits due to their high quality factors and frequency stability. In a series application (often described by Butterworth-Van Dyke equivalent circuit models) these crystal devices have a detectable current output proportional to the motional behavior of the crystal. The piezoelectric effect in these materials generates electric current due to an applied mechanical stress, and conversely applying an electric current to these crystals induces mechanical stress.

It is more convenient to control laboratory function generators, power supplies, and oscilloscopes with respect to voltage, so the current output of the piezoelectric device must be appropriately converted. A load resistor may be used to transform current to voltage, but this adds a DC offset and ground noise to the oscillating resonator signal. Also, including resistors in series with a piezoelectric device lowers

the effective quality factor by increasing damping in the system. To avoid excessive damping, the required load resistor would be too small to provide a sufficient gain for accurately measuring an output voltage amplitude. Instead, a simple transimpedance amplifier setup can be used to transform the piezoelectric current output to a voltage, as described by Bajaj [16], for example. Transimpedance amplifiers are commonly used in similar circuits to detect small currents from photodiodes or other capacitive sensors.

There are two important stipulations regarding the phase of the transimpedance amplifier output. First, the physical motion of the resonator can be described by the *voltage* across the piezoelectric crystal, not the *current* through it. By the capacitive nature of the device, the current output of the crystal is proportional to the time-derivative of the voltage across it. To obtain the resonator voltage, $V_{crystal}$, an integrator may be used on the transformed current output of the crystal, $I_{crystal}$ (as described by Bajaj [16], which also requires a high-pass filter to eliminate DC offset), or more simply it can be noted that for sinusoidal signals the current will *lead* the voltage by 90°. Second, the transimpedance amplifier itself will additionally contribute a 180° phase *lag* to the signal, since the output voltage of the transimpedance amplifier, V_{TI}, is proportional to the input current $I_{crystal}$ with opposite sign. Table 3.1 summarizes the phase-offsetting that occurs as the input signal propagates through the resonator and transimpedance amplifier below resonance, near resonance, and above resonance. The resulting phase offset of V_{TI} will simply require that the design variable ϕ be additionally offset by $-90°$ to match the theoretical results above. This phase offset is only a concern for the single resonator circuit, since the two resonator design has equivalent offsets on both channels such that the relative phase difference between signal branches is simply ϕ.

In the prototype circuits presented here, the input signal voltage is split equally between the two signal branches, which are isolated from each other by a pair of buffer operational amplifiers. Similarly, the outputs of each branch are isolated and summed back together with buffers and a summing amplifier. The individual branch voltages

Table 3.1. Phase Offsets of Piezoelectric Crystal Resonator and Transimpedance Amplifier.

	$V_{crystal}$	$I_{crystal}$	V_{TI}
Below Resonance	0°	90°	−90°
Near Resonance	−90°	0°	−180°
Above Resonance	−180°	−90°	−270°

are measured independently with another set of buffered outputs. It is important to isolate the signal branches and measurements using buffers because the resonators must remain uncoupled from other signal paths to match the corresponding system block diagram.

3.1.3 Phase Shifting Element

There are several ways to implement a phase shifting element in electrical hardware. Signal interference filters at high radio frequencies use transmission line differences, which is typically seen as varied microstrip trace lengths in FR-4 copper-cladded printed circuit boards (PCB). As previously stated, this technique does not scale well to lower frequency ranges, but a trial circuit is evaluated here to confirm this claim.

A constant width microstrip trace was designed in an FR-4 copper PCB using a wide serpentine pattern for compactness, as seen in Figure 3.1. This was then tested by connecting a function generator and oscilloscope to the microstrip through BNC cables. Supplying a 50 MHz input to this simple transmission line, it was noted that the combined effect of 2 ft of BNC cables and 15 in of total microstrip length were only able to phase shift the signal by about 107°. This large transmission line setup is too long to suit lower-frequency applications. To generate a phase shift of 180° in microstrip alone, it was determined that a total length of about 60 in would be required. Also, making these long transmission lines more compact through

special patterns causes increased inductance of the transmission line. Although these transmission lines are easy to design, they cannot be continuously tuned as preferred for this work.

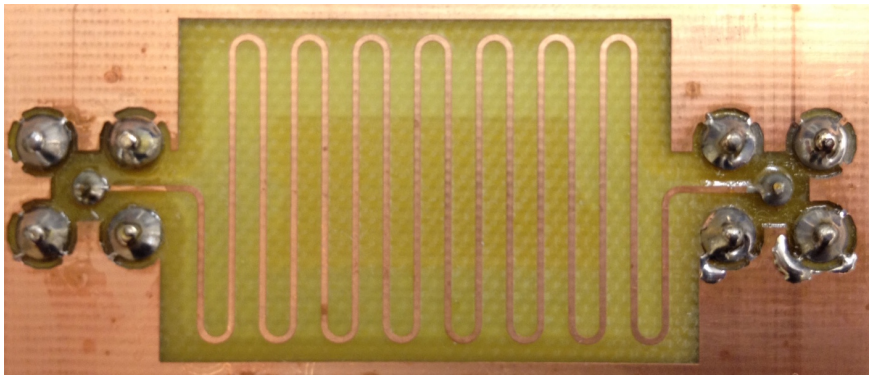

Figure 3.1. Serpentine microstrip trace used to test the capability of transmission lines for the phase-shifting element in the experimental signal interference systems at 50 MHz. It was determined that the combined effect of BNC cables, microstrip, and junctions did not sufficiently phase shift the signal for use in these lower-frequency signal interference systems.

Lumped element capacitors, inductors, and resistors are used in numerous filter configurations for their phase-shifting properties, including low-pass, high-pass, band-pass, band-stop, and delay equalizer circuits. Though these phase-shifting elements can be scaled to lower frequencies without drastically affecting component size, they typically attenuate the signal. Phase shifting with low-pass, high-pass, or band-pass filters attenuate the voltage signal directly by requiring operation near or above the filter cutoff frequency. Delay equalizers and passive all-pass circuits have ideally flat amplitude responses, but they include inductor and capacitor architectures that are costly and non-ideal at high frequencies. These passive devices commonly rely on accurately matched component values, which increases manufacturing cost and makes tuning the phase shift more difficult to control.

An active all-pass filter circuit leverages the ideally constant amplitude response of the passive all-pass and delay equalizers, but without inductive elements. This

simplifies the design and allows for the phase shift to be easily tuned from 0° to 180° by varying a resistor or capacitor element. It should be noted that all of the phase shifting techniques discussed in this section are frequency dependent. Other phase shifting methods were considered, such as phase-locked loops (PLLs), but these proved far too costly and complex for a simple proof-of-concept signal interference system. Therefore, the ideal phase shifter ϕ is realized here with an active all-pass filter: a high-pass RC filter is placed on the non-inverting pin of an operational amplifier, and equal input and gain-setting resistors (R_I and R_G, respectively) are placed on the inverting pin, as seen in [23]. The basic circuit diagram for this setup is shown in Figure 3.2.

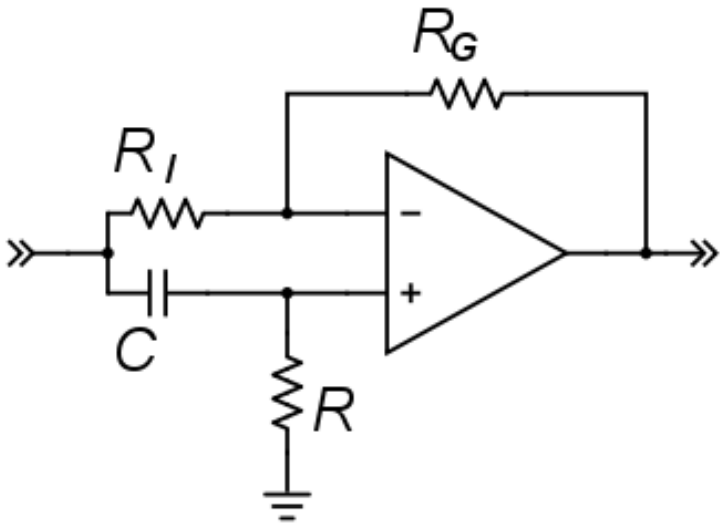

Figure 3.2. Circuit diagram of the active all-pass filter with an RC high-pass filter on the non-inverting input and equal input resistor (R_I) and gain-setting resistor (R_G) on the inverting input. This circuit ideally passes all frequencies with equal amplitude, and it employs a phase shift near the cutoff of the high-pass RC filter.

The all-pass design can be used to phase shift the signal from 0° to 180° by altering the RC filter values according to $\phi = 2\arctan(1/2\pi fRC)$ without affecting

the amplitude response (hence the name "all-pass"). For example, a $\phi = 45°$ phase shift may be obtained with a $C = 100$ pF capacitor at a frequency of $f = 50$ MHz using a resistance of about $R = 76.85\ \Omega$. An inverting operational amplifier with a gain of -1 can also be switched into the circuit before the all-pass phase shifter to contribute an additional 180° of phase lag to map the entire range of ϕ from $-180°$ to 180°.

The gain parameter G is realized with a non-inverting operational amplifier with a nominal gain of 1. The G parameter is easily tuned through varying the feedback resistance of the amplifier.

3.2 Simulations in SPICE Software

An added benefit of generating an experimental proof-of-concept system in analog circuitry is that many simple circuit elements can be rapidly simulated before building and testing a physical implementation. The circuits developed here were simulated first using SPICE-based software with circuit element models to ensure the validity of these analog designs. The circuits in this study were simulated using the free version TINA-TI SPICE-based software available from Texas Instruments (`www.ti.com/tool/tina-ti`).

3.2.1 Single Resonator System

The one resonator simulation approach is shown in Figure 3.3. The input signal is split and kept isolated by ideal buffer amplifiers (+1), and the individual branch voltages are also measured through buffers. The resonator output is transformed to a voltage by the transimpedance amplifier (TI) and the second signal branch included a switchable inverter (-1), an all-pass phase shifter (ϕ), and a non-inverting gain amplifier (G).

Based on the all-pass relationship given above, values of RC were chosen to yield the same characteristic ϕ values as in Figure 2.3. The second-order response of the

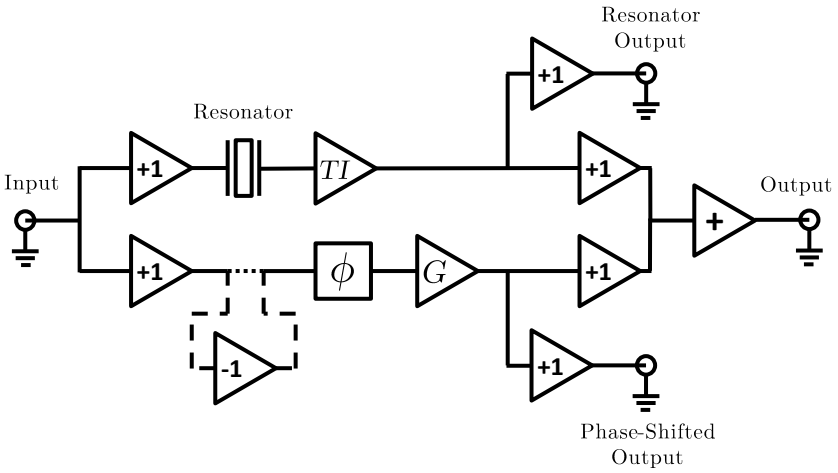

Figure 3.3. Schematic of the simulated one resonator system using ideal buffer amplifiers for power splitting, power combining, and isolated output measurements. The resonator is a piezoelectric crystal and the phase shifter ϕ is an ideal all-pass filter. The resonator output is transformed to voltage using a transimpedance amplifier (TI) and the amplitudes of the two branches are matched with a gain G. An inverting amplifier section (line with long segments) can be inserted into the signal path between the input and phase shifter (line with short segments) to incorporate an additional 180° of phase lag.

piezoelectric crystal resonator was simulated using a series RLC network with a natural frequency of $f = 50$ MHz and a Q-factor of 10,000, according to $2\pi f = 1/\sqrt{LC}$ and $Q = (\sqrt{L/C})/R$ with R assumed to be 50 Ω. Figure 3.4 shows the simulated output responses of the above control setup with ideal active and passive components.

These results show that the simulated system qualitatively matches the modeled output response for the setup described above. The primary difference between simulated and theoretical results is the $-90°$ resonator branch phase offset mentioned in Table 3.1, which causes $\phi = 180°$ and $\phi = 0°$ to be constructive and destructive, respectively, instead of $\phi = -90°$ and $\phi = 90°$ as predicted from the model. Although this proposed design is not optimized for a specific application, it is clear from these simulation results that the fundamental operation of this analog circuit is sufficiently understood and described by the system diagram in Figure 2.1 and

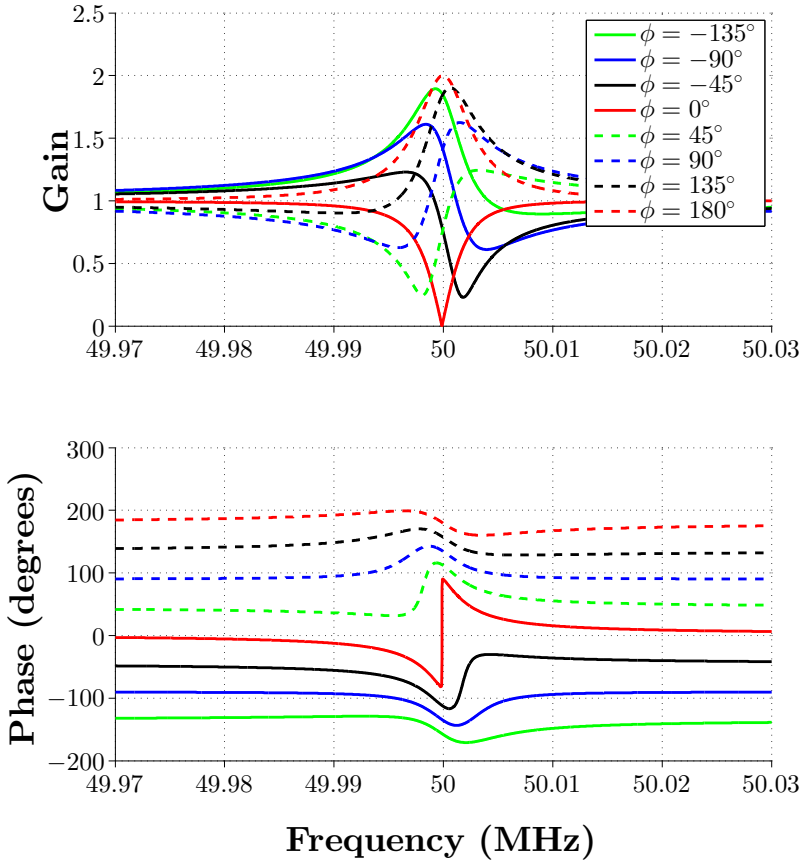

Figure 3.4. Simulation frequency responses for characteristic values of ϕ using operational amplifiers and passive components. Here a series RLC is used to model the second order response of the piezoelectric crystal resonator with a Q-factor of 10,000 and a natural frequency of 50 MHz.

the non-dimensional model of Equation (2.12). By using passive and active components and a piezoelectric crystal resonator the modeled system can now be confidently constructed using the architecture of Figure 3.3.

3.2.2 Two Resonator System

The two resonator mathematical model was simulated using the circuit architecture shown in Figure 3.5. For the first resonator, a nominal natural frequency of

$\omega_{n1} = 50$ MHz was chosen, which was again represented in the SPICE software using an equivalent RLC circuit with a Q-factor of 10,000. The second resonator's natural frequency was varied near a nominal 50 MHz value to yield α values of 0.9999 and 1.0001 by adjusting the L and C values of its RLC equivalent circuit.

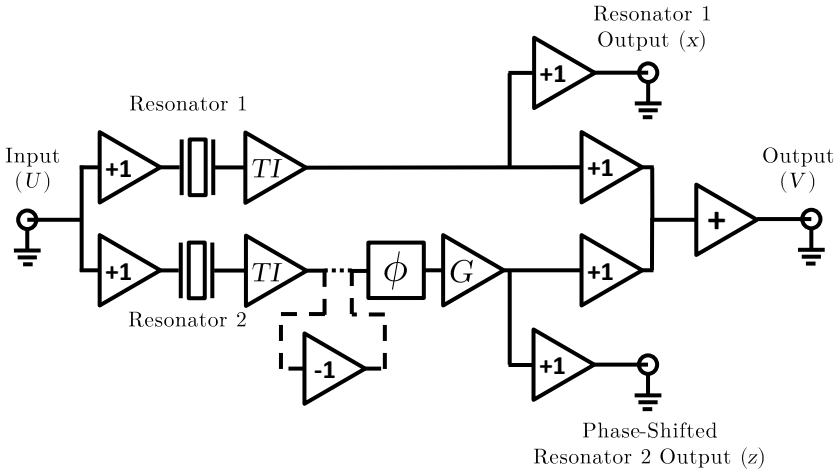

Figure 3.5. Schematic of the simulated two resonator system, which includes an additional resonator and transimpedance amplifier in the second signal path. The phase shift ϕ and gain G are still design variables along with the relative detuning ratio α of the natural frequencies of the resonators. It is assumed that both resonators have the same quality factor.

Two results of these simulations are shown in Figure 3.6. Note that plots (c) and (d), as indicated in the figure's key, are reflective of the corresponding model predictions shown in Figure 2.5. The same qualitative band-pass and notch response shapes are observed here in the simulated system, confirming the utility of this simple circuit as a proof-of-concept design.

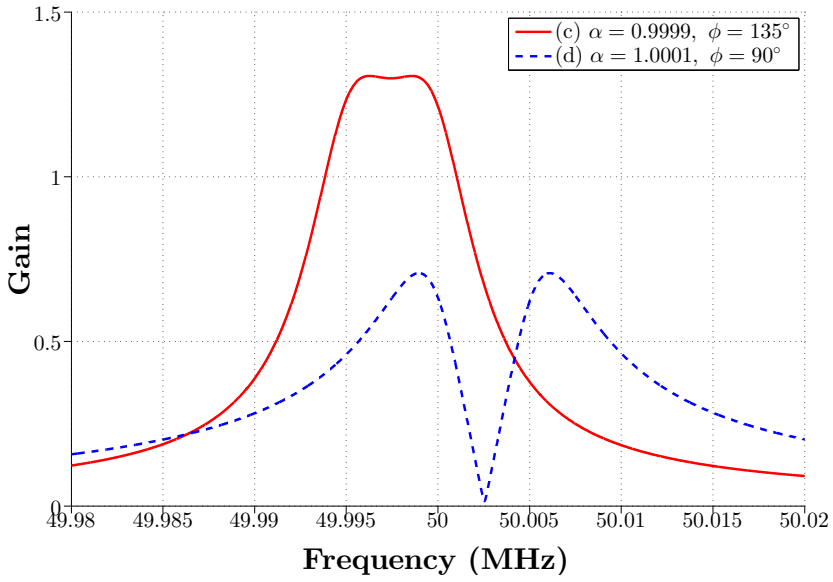

Figure 3.6. Simulation frequency responses of the two resonator signal interference system matching the noted results of Figure 2.5, where (c) is a band-pass-type response and (d) shows a combination of resonance and cancellation.

CHAPTER 4. EXPERIMENTAL RESULTS

To implement the prototype design described above, an appropriate operational amplifier was chosen for all active components. The LMH6609 from Texas Instruments is an ultra-wideband voltage feedback operational amplifier that is unity gain stable and has a small-signal -3 dB bandwidth well above the desired 50 MHz operating range. The LMH6609 is also well designed for high-speed buffering and transimpedance applications, making it appropriate for the active devices in this circuit. The next step in designing this circuit was to choose an appropriate piezoelectric crystal with a resonant response of the form of Equation (2.1). The CX3225GB bulk-mode 50 MHz surface-mount quartz crystal from Kyocera was used for this application, most of which had a resonant frequency near 49.992 MHz when tested.

Physical circuits were built according to the simulation architectures presented above using KiCad open source PCB design software (`http://kicad-pcb.org/`). Special care was given to reducing the trace lengths between components in the signal paths. Standard size 0603 or 0805 commercially-available passive components were used for compactness and better signal propagation characteristics as compared to through-hole components. Decoupling capacitors were included for each operational amplifier according to the LMH6609 specifications, and BNC junctions were added for interfacing with the laboratory signal source, power supplies, and measurement equipment. A ground plane on the PCB and coaxial BNC cables were utilized for noise-reduction and signal integrity purposes. An example of these PCB circuits is shown in Figure 4.1 for the two resonator system.

The DC power supplies employed here were two Agilent E3645A that provide +5V, -5V, and ground to the circuit. The sinusoidal input was provided at 200 mV peak-to-peak amplitude from an 80 MHz Agilent 33250A function generator. The outputs of the circuit were then measured on a 1 GHz, 4-channel Agilent DSO8104A

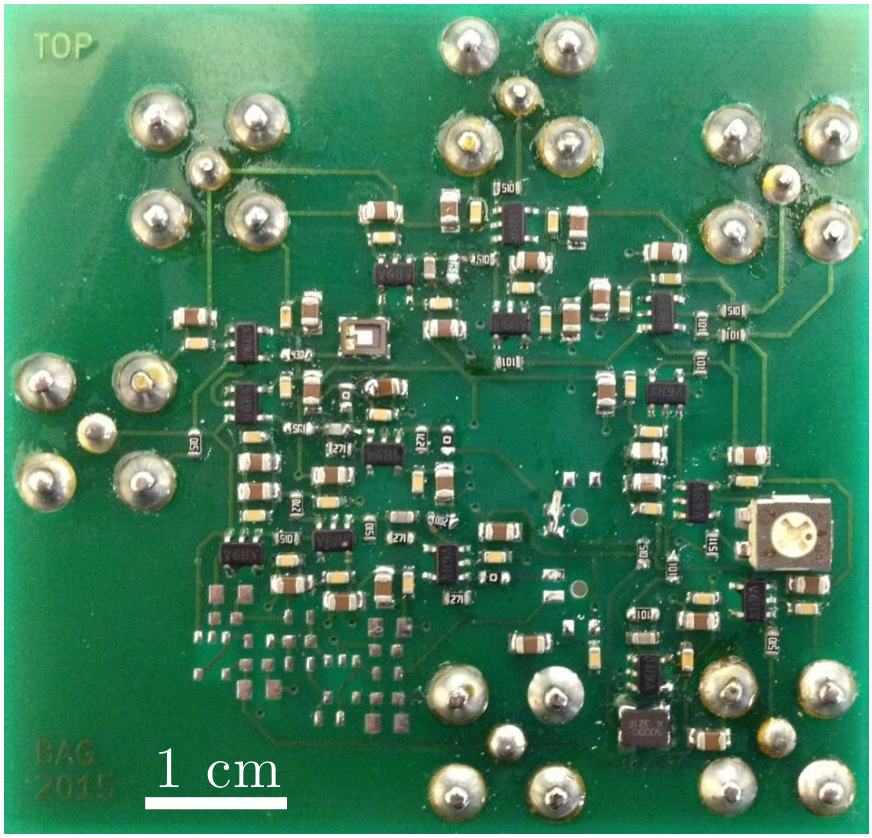

Figure 4.1. An example of the types of PCB proof-of-concept circuits built in this work. This depiction is the two resonator electromechanical circuit, according to the experimental schematic of Figure 4.5.

oscilloscope. The experimental setup was controlled by a LabVIEW program using GPIB connections and drivers (obtained from National Instruments and Agilent). Each device was characterized by sweeping the input frequency within a tight range of frequencies around resonance, with the source and oscilloscope both set to 50 Ω impedance.

4.1 Single Resonator System

The experimental schematic for the single resonator circuit is depicted in Figure 4.2. The outputs of this circuit were measured without averaging, and LabVIEW recorded amplitude and phase information for each channel at 50 Hz increments

between 49.965 MHz and 50.015 MHz. The all-pass phase-shifter included a constant 22 pF capacitor and incorporated a 1 kΩ variable resistor as the tuning element. By adjusting the resistor position, roughly similar characteristic values of ϕ as above were evaluated. In the results that follow, the reported ϕ values were the *relative* phases between branches, which allowed the -90° transimpedance phase offset to be ignored. To ensure exact amplitude matching ($G = 1$) between the two signal branches at resonance, a second 1 kΩ variable resistor was included on the gain amplifier to adjust the phase-shifted branch amplitude.

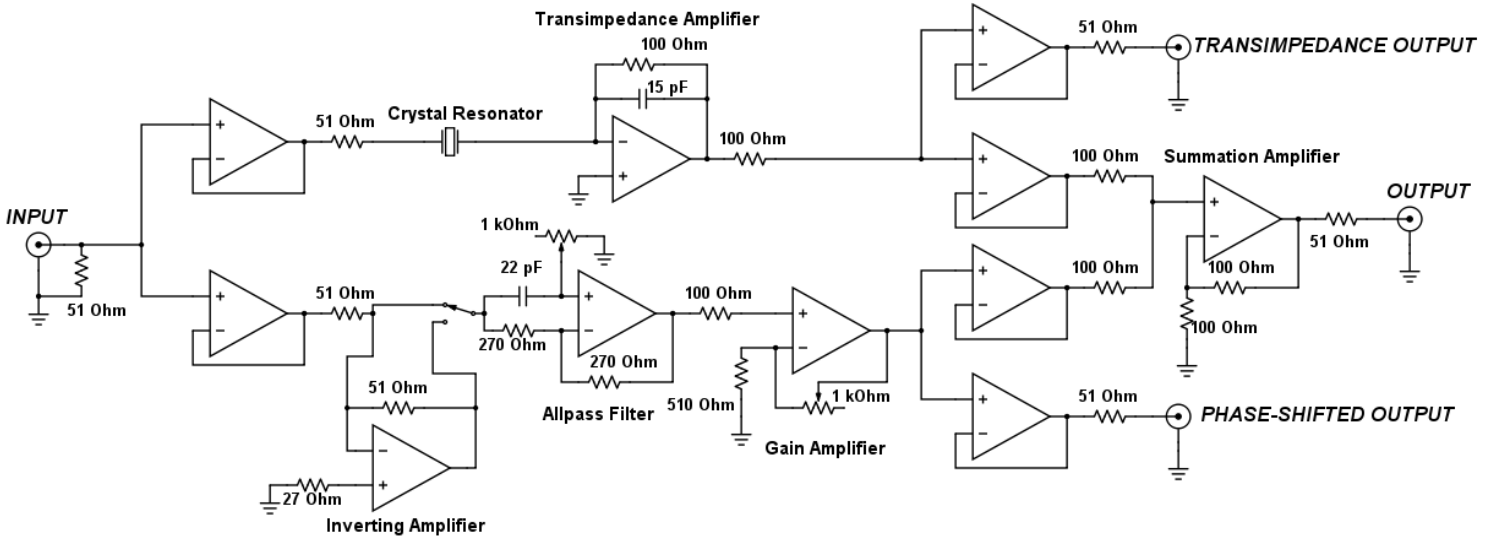

Figure 4.2. Schematic of the single resonator experimental test circuit, where the input was provided by an Agilent 33250A function generator and the outputs were measured using an Agilent DSO8104A oscilloscope. Power at +5V, -5V, and ground was provided by two Agilent E3645A DC supplies. All operational amplifiers were LMH6609 by Texas Instruments, and the quartz crystal resonator was a Kyocera CX3225GB at 50 MHz. The inverting amplifier was switched into the circuit to provide an extra 180° phase shift. Power supply pins and decoupling capacitors not shown.

Frequency sweeps were performed for four all-pass resistor settings and are shown in Figure 4.3. The data from these experimental sweeps was processed in order to estimate the phase ϕ, Q-factor, natural frequency f_n, and gain G. These characteristic values were then substituted into the mathematical model to produce the model curves in Figure 4.3. The purpose of this process was to demonstrate the applicability of the model as a set of design equations rather than simply curve-fitting the model to the data (as in a least squares regression, for example). Table 4.1 details the experimentally-measured parameters that these model curves were based on.

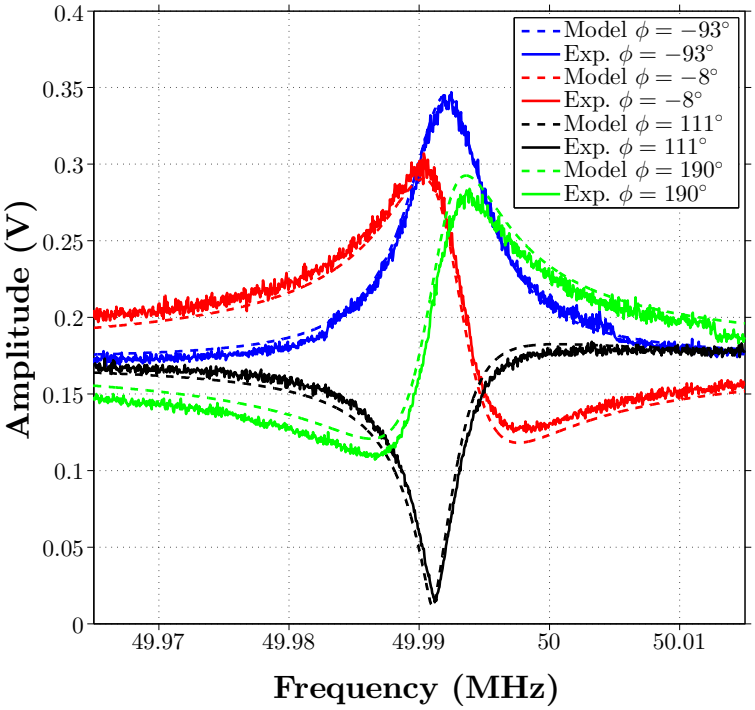

Figure 4.3. Frequency responses of the experimental and modeled single resonator signal interference output. By adjusting the all-pass variable resistor, several values of ϕ were obtained to tune the circuit behavior. The model curves were generated by approximating system parameters from the experimental results, as shown in Table 4.1.

The qualitative nature of the experimental output response matched expectation from the mathematical model for each value of ϕ. However, there was some slight quantitative disagreement between the model and experiment. This likely arose from

Table 4.1. Experimentally-Measured Parameters for Generating the Single Resonator Model Curves in Figure 4.3.

ϕ	Q	f_n (MHz)	G
$-93°$	8063	49.99190	1.01023
$-8°$	8129	49.99170	1.00762
$111°$	8195	49.99175	1.00551
$190°$	8263	49.99180	1.01082

the discrete nature of the experimental results (50 Hz increments), which caused the measured parameters of Table 4.1 to be approximate. Since the model curves here were designed to the experimental measurements, the agreement between model and experiment in Figure 4.3 is reasonable.

A small amount of noise was also seen in the experimental system (on the order of a few mV), likely caused by the function generator and DC supplies. This noise could be easily smoothed out using the oscilloscope's averaging functions or by adding a low-pass filter with sufficiently high cutoff on the circuit output.

To be certain that the experimental device was well modeled by theory, it was important to determine if the device was operating in a linear amplitude and phase range. This was confirmed by exciting the device with higher and lower input amplitudes and observing the similarity of the gain and phase of the outputs at each amplitude. Figure 4.4 shows the gain of the circuit (output amplitude with respect to input amplitude) as well as its phase for the constructive interference case ($\phi = -90°$). Clearly all three distinct input amplitudes tracked the same output response, indicating the device was operating in a linear range. Therefore, the experimental proof-of-concept circuit devised here was an appropriate physical representation of the proposed theoretical system.

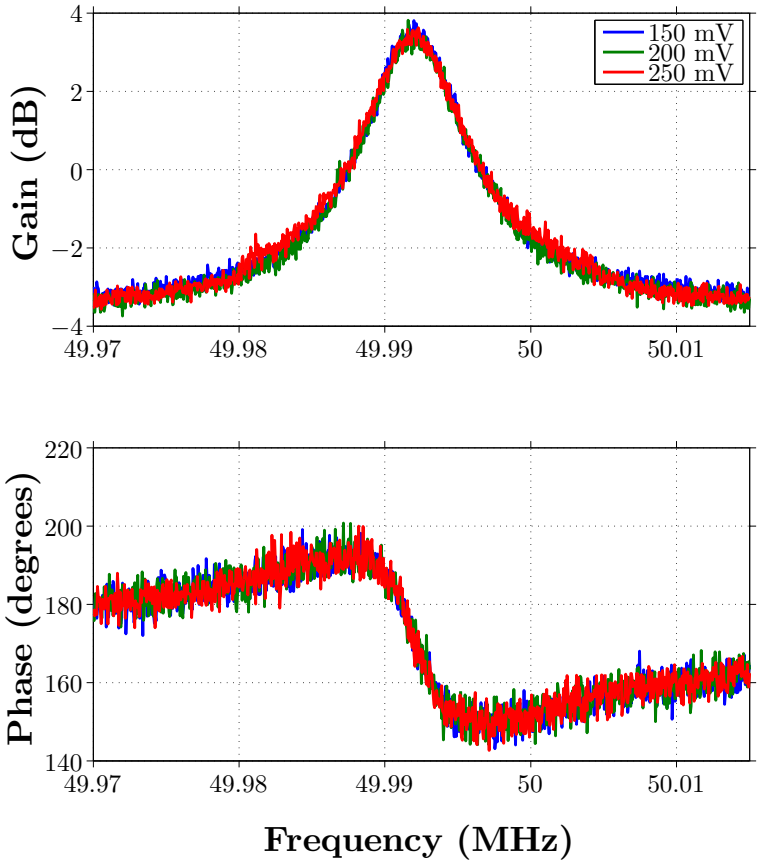

Figure 4.4. Three frequency responses of the signal interference test circuit at the constructive interference value of $\phi = -90°$. The input amplitude was adjusted above and below the nominal 200 mV input in order to test the linearity of this circuit. The gain and phase plots tracked the same response for all three values of input magnitude, so the circuit was operating in a linear response range.

4.2 Two Resonator System

The experimental setup for the two resonator system was the same as the single resonator, with the exception that the input was swept in 100 Hz increments from 49.9775 MHz to 50.0005 MHz. Also, a 4-point averaging setup was implemented in the oscilloscope data recording scheme to reduce measurement noise. The experimen-

tal schematic is shown in Figure 4.5, where a second resonator and transimpedance amplifier were added to the second signal branch.

As in the single resonator trials, the variable gain-setting resistor was set to match the amplitude between the two channels ($G = 1$). Again, the variable phase-setting resistor was roughly set to yield similar characteristic ϕ values, and the experimental results were evaluated to determine appropriate model design parameters for comparison.

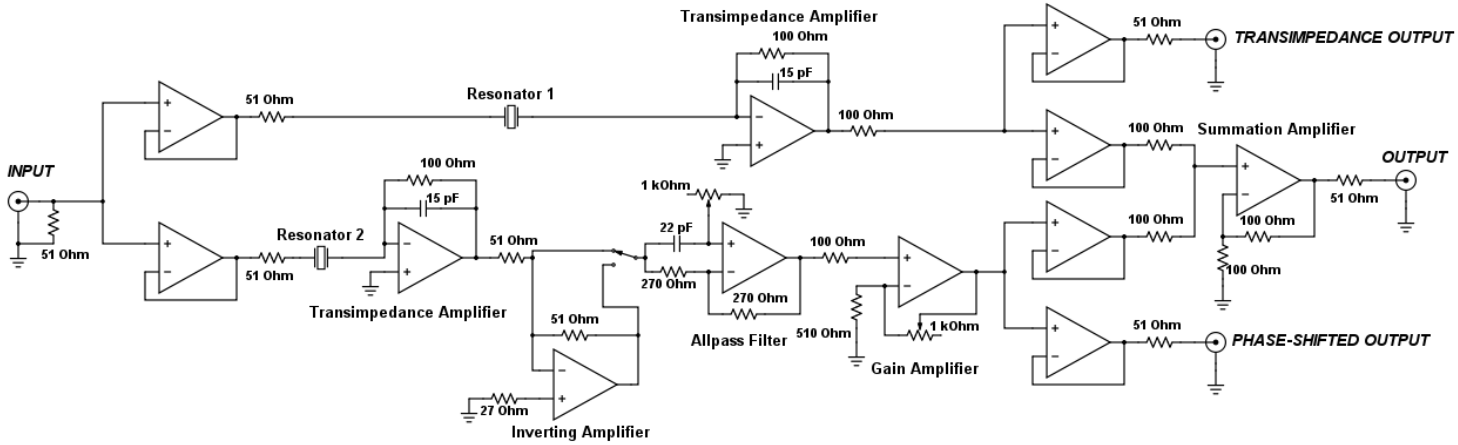

Figure 4.5. Schematic of the two resonator experimental test circuit. The input was provided by an Agilent 33250A function generator and the outputs were measured using an Agilent DSO8104A oscilloscope. Power at +5V, -5V, and ground was provided by two Agilent E3645A DC supplies. All operational amplifiers were LMH6609 by Texas Instruments, and the quartz crystal resonators were Kyocera CX3225GB at 50 MHz. The inverting amplifier was switched into the circuit to provide an extra 180° phase shift. Power supply pins and decoupling capacitors not shown.

4.2.1 Nominal Frequency Detuning of $\alpha \approx 1$

For the first trial, shown in Figure 4.6, the two resonators were tested without alteration such that α was approximately 1. The measured parameters that were used to generate the model curves are presented in Table 4.2.

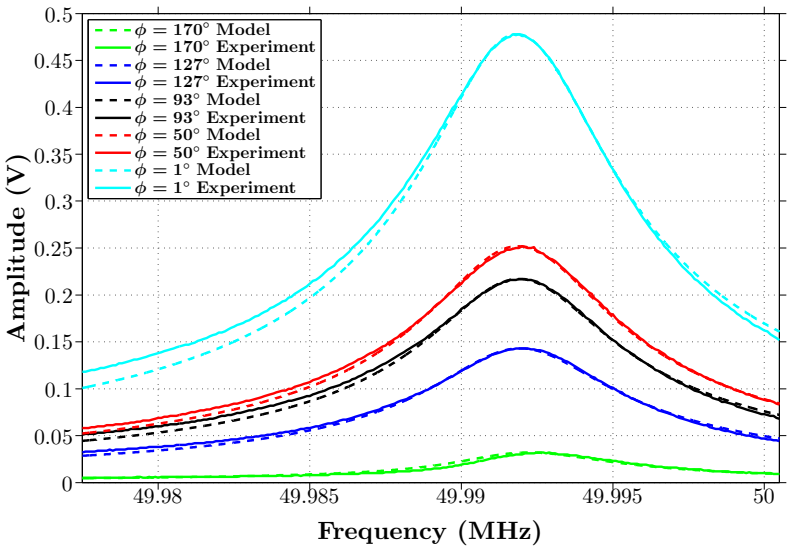

Figure 4.6. Frequency responses of the experimental and modeled two resonator signal interference output with $\alpha \approx 1$. By adjusting the all-pass variable resistor, several values of ϕ were obtained to tune the circuit behavior. The model curves were generated by approximating system parameters from the experimental results, as shown in Table 4.2.

The experimental and modeled results shown here were again qualitatively similar, though there was still a slight amount of disagreement due to the discrete data parameter estimation described above (which was more significant here due to decreased frequency resolution from 50 Hz to 100 Hz increments). The 4-point oscilloscope averaging seemed to have eliminated most of the noise observed in the single resonator trials.

Table 4.2. Experimentally-Measured Parameters for Generating the $\alpha \approx 1$ Two Resonator Model Curves in Figure 4.6.

ϕ	Q_1	Q_2	f_{n1} (MHz)	f_{n2} (MHz)	G	α
170°	7691	8332	49.99185	49.99170	1.00823	0.999997
127°	7691	8195	49.99190	49.99170	1.00000	0.999996
93°	7691	8332	49.99190	49.99170	1.00823	0.999996
50°	7811	8332	49.99195	49.99175	1.00000	0.999996
1°	7691	8473	49.99195	49.99175	1.01240	0.999996

4.2.2 Nominal Frequency Detuning of $\alpha \approx 0.9999$

Next, the two resonator system was evaluated with $G = 1$ and $\alpha \approx 0.9999$. Since commercial quartz crystals were not available at such a small frequency offset as those required in this experiment, and because the manufacturing tolerances of these crystals were tighter than the desired frequency detuning, the resonators used in this experiment were modified to give the desired offset. From a mechanical standpoint, the natural frequency of the crystals depends primarily on the effective stiffness k and mass m [see Equation (2.2)]. Since the stiffness of these piezoelectric resonators is difficult to modify after production, the effective mass was changed. This was accomplished with a custom-mounted thermal inkjet picojet printing system provided by Hewlett-Packard, which applied small amounts of inert polystyrene to the surface of the crystal. Figure 4.7(a) shows the quartz resonator with the cover removed, and Figure 4.7(b) shows the resonator with mass added. This process is not detailed here, as it is the operating principle employed in many linear (and nonlinear) mass sensing systems [16].

Figure 4.8 shows the trials for $\alpha \approx 0.9999$, which were performed by lowering the second resonator's natural frequency through inkjet-based mass-deposition. The measured parameters for generating the model curves are detailed in Table 4.3.

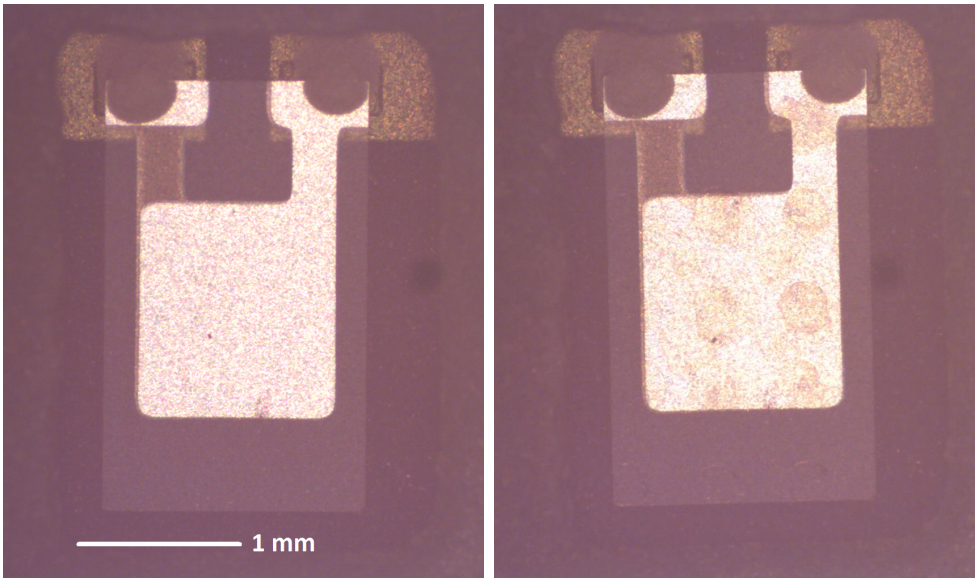

(a) (b)

Figure 4.7. Images of the Kyocera CX3225GB 50 MHz bulk-mode quartz resonator (a) with the cover removed and (b) after depositing drops of polystyrene (brown spots on the electrode).

Table 4.3. Experimentally-Measured Parameters for Generating the $\alpha \approx 0.9999$ Two Resonator Model Curves in Figure 4.8.

ϕ	Q_1	Q_2	f_{n1} (MHz)	f_{n2} (MHz)	G	α
160°	7811	7574	49.99195	49.98555	1.00410	0.999872
127°	7691	7461	49.99195	49.98565	1.02058	0.999874
89°	7691	7461	49.99195	49.98565	1.00000	0.999874
38°	7811	7461	49.99195	49.98565	1.00000	0.999874
−11°	7811	7351	49.99190	49.98565	1.00000	0.999875

These results show the development of the aforementioned band-pass-type responses for sufficiently large ϕ values. Here the experimental and model results also match reasonably well, with slightly more deviation than the $\alpha \approx 1$ case, which is primarily caused by the inability of the oscilloscope to measure ϕ values as accurately as desired.

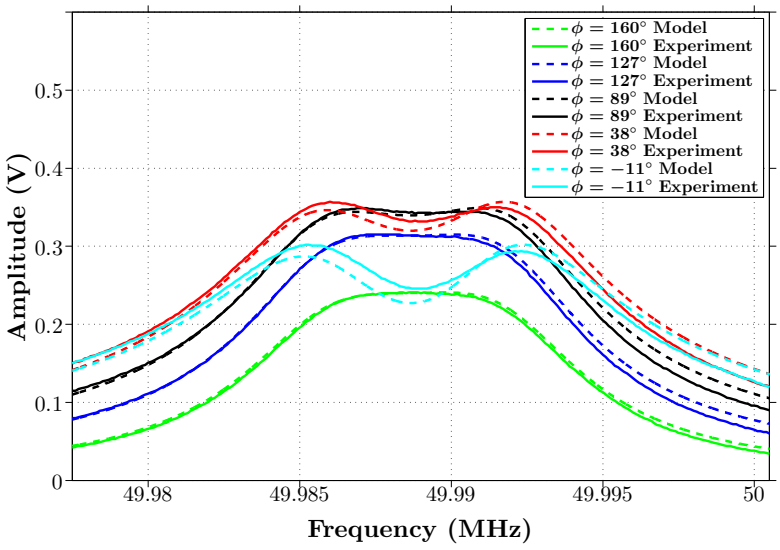

Figure 4.8. Frequency responses of the experimental and modeled two resonator signal interference output with $\alpha \approx 0.9999$. By adjusting the all-pass variable resistor, several values of ϕ were obtained to tune the circuit behavior. The model curves were generated by approximating system parameters from the experimental results, as shown in Table 4.3.

4.2.3 Nominal Frequency Detuning of $\alpha \approx 1.0001$

Finally, this system was evaluated with $G = 1$ and $\alpha \approx 1.0001$, as shown in Figure 4.9. These trials are performed by lowering the first resonator's natural frequency relative to the second resonator through inkjet mass-printing. The measured parameters for generating the model curves are detailed in Table 4.4.

These results show the development of the aforementioned combinations of resonance and anti-resonance behaviors. Here, the experimental and model results match quite well, except for the $\phi = 96°$ case in which it was observed that a small amount damping in the laboratory BNC junctions and cables may have prevented the experimental results from achieving the same level of amplitude-canceling behavior as the model predicts.

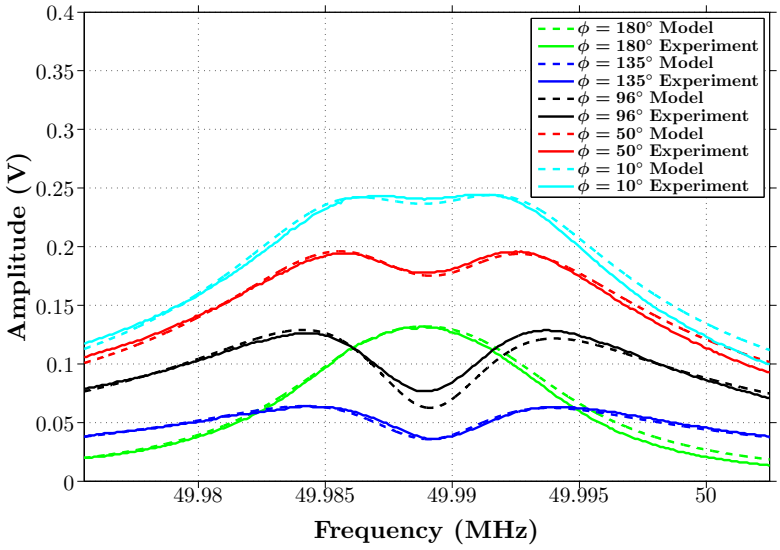

Figure 4.9. Frequency responses of the experimental and modeled two resonator signal interference output with $\alpha \approx 1.0001$. By adjusting the all-pass variable resistor, several values of ϕ were obtained to tune the circuit behavior. The model curves were generated by approximating system parameters from the experimental results, as shown in Table 4.4.

Table 4.4. Experimentally-Measured Parameters for Generating the $\alpha \approx 1.0001$ Two Resonator Model Curves in Figure 4.9.

ϕ	Q_1	Q_2	f_{n1} (MHz)	f_{n2} (MHz)	G	α
180°	5375	5375	49.9863	49.99165	0.98795	1.000107
135°	5375	5494	49.9863	49.99165	0.97605	1.000107
96°	5493	5375	49.9863	49.99165	0.97633	1.000107
50°	5375	5375	49.9865	49.99170	0.97590	1.000104
10°	5318	5434	49.9862	49.99170	0.98182	1.000110

CHAPTER 5. CONCLUSIONS

Two mechanical resonance control systems were modeled to show continuously-tunable frequency response behaviors. These systems demonstrate signal interference characteristics in which input signal frequencies are selectively amplified or canceled through phase-shifted combinations at the output.

Generalized first-principles dynamic models were developed in Chapter 2 through a process of non-dimensionalization beginning with linear second-order differential equations. Section 2.2 evaluated a signal interference system with one high-Q resonator, and Section 2.3 established a two resonator structure. Model limitations were discussed in Section 2.4, including the assumption of linear resonance responses.

In Chapter 3, these mathematical models were used to construct an ideal proof-of-concept system in electromechanical circuitry to demonstrate an application of signal interference using high-Q resonant elements. Section 3.1 detailed the choices of piezoelectric resonators and all-pass phase shifting circuitry, and SPICE simulations were performed in Section 3.2. Prototype experimental circuits were then developed in Chapter 4 to show the qualitative nature of the proposed resonant systems. These circuit architectures were implemented using PCB technology and commonly-available discrete components. The one resonator structure was tested in Section 4.1, and inkjet mass deposition enabled natural frequency shifting for the two resonator designs in Section 4.2.

The experimental circuits matched the model predictions well as a proof-of-concept, so the generalized theoretical models derived in Chapter 2 adequately describe the dynamics of this real control system. As such, the model equations may be appropriately utilized in a design context for any combination of Q-factors, natural frequencies, relative gains, and relative phase offsets for given Lorentzian resonant elements in these signal interference topologies. In general, the proposed control systems can

be expanded to a wider range of feedforward or signal-interference-based frequency response tuning.

The primary motivation of this work was to combine mechanical resonance with feedforward control as achieved through signal interference and to develop analytical models to predict the observable frequency response tuning behaviors of these architectures. The control topology described here does not seek to design specific resonant elements, but instead to develop a means to shape frequency domain behaviors by encapsulating resonators in feedforward systems. This work therefore serves as a step toward understanding on-chip system integration for arrays of micro- and nanosystems. One recommendation for future work in this area is to connect arrays of the one and two resonator devices in parallel to generate more complex frequency response behavior with attendant tuning and control. The electromechanical circuits built in this work could ideally be linked together in a modular system approach, or enhanced tuning behaviors may be achieved with additional feedforward signal branches.

Observations of nonlinear frequency response behaviors are routine and often useful in M/NEMS devices. Future implementations of the analytical models of this work should investigate nonlinear resonance behaviors. Specifically, it should be determined how some common resonator nonlinearities might impact tuning and interference output amplitudes in this form of feedforward control. This work has facilitated the application of signal interference concepts outside electrical filtering domains, and the models here should be further improved to understand the extent to which signal interference can be utilized as a tool for resonant control.

LIST OF REFERENCES

LIST OF REFERENCES

[1] J. F. Rhoads, S. W. Shaw, and K. L. Turner. Nonlinear dynamics and its applications in micro- and nanoresonators. *Journal of Dynamic Systems, Measurement, and Control*, 132(03):034001, 2010.

[2] S. L. Calvert, Y. Shen, A. B. Sabater, S. Mohammadi, and J. F. Rhoads. Towards a comprehensive model for a resonant nanoelectromechanical system. *Journal of Micromechanics and Microengineering*, 25(9):095010, 2015.

[3] L.-H. Hsieh and K. Chang. Compact, low insertion-loss, sharp-rejection, and wide-band microstrip bandpass filters. *IEEE Transactions on Microwave Theory and Techniques*, 51(4):1241–1246, 2003.

[4] R. Gomez-Garcia, J. I. Alonso, and C. Briso-Rodriguez. On the design of high-linear and low-noise two-branch channelized active bandpass filters. *IEEE Transactions on Circuits and Systems II: Analog and Digital Signal Processing*, 50(10):695–704, 2003.

[5] R. Gomez-Garcia and J. I. Alonso. Design of sharp-rejection and low-loss wide-band planar filters using signal-interference techniques. *IEEE Microwave and Wireless Components Letters*, 15(8):530–532, 2005.

[6] M. A. Sanchez-Soriano, E. Bronchalo, and G. Torregrosa-Penalva. Compact UWB bandpass filter based on signal interference techniques. *IEEE Microwave and Wireless Components Letters*, 19(11):692–694, 2009.

[7] D. Psychogiou, D. Peroulis, R. Loeches-Sanchez, and R. Gomez-Garcia. Analog signal-interference narrow-band bandpass filters with hybrid transmission-line/SAW-resonator transversal filtering sections. *2015 IEEE International Symposium on Circuits and Systems (ISCAS)*, pages 281–284, 2015.

[8] C. Rauscher. Microwave active filters based on transversal and recursive principles. *IEEE Transactions on Microwave Theory and Techniques*, 33(12):1350–1360, 1985.

[9] C. Rauscher. Two-branch microwave channelized active bandpass filters. *IEEE Transactions on Microwave Theory and Techniques*, 48(3):437–444, 2000.

[10] M. A. Sanchez-Soriano and J.-S. Hong. Reconfigurable lowpass filter based on signal interference techniques. *2011 IEEE MTT-S International Microwave Symposium Digest (MTT)*, pages 1–4, 2011.

[11] R. Gomez-Garcia, M.-A. Sanchez-Soriano, K.-W. Tam, and Q. Xue. Flexible filters: reconfigurable-bandwidth bandpass planar filters with ultralarge tuning ratio. *IEEE Microwave Magazine*, 15(5):43–54, 2014.

[12] E. J. Naglich, D. Peroulis, and W. J. Chappell. Low-order filter response enhancement in reconfigurable resonator arrays. *IEEE Transactions on Microwave Theory and Techniques*, 61(12):4387–4395, 2013.

[13] C. Rauscher. Varactor-tuned active notch filter with low passband noise and signal distortion. *IEEE Transactions on Microwave Theory and Techniques*, 49(8):1431–1437, 2001.

[14] V. Kumar, J. W. Boley, Y. Yang, H. Ekowaluyo, J. K. Miller, G. T.-C. Chiu, and J. F. Rhoads. Bifurcation-based mass sensing using piezoelectrically-actuated microcantilevers. *Applied Physics Letters*, 98(15):153510, 2011.

[15] R. L. Harne and K. W. Wang. Robust sensing methodology for detecting change with bistable circuitry dynamics tailoring. *Applied Physics Letters*, 102(20):203506, 2013.

[16] N. Bajaj, A. B. Sabater, J. N. Hickey, G. T.-C. Chiu, and J. F. Rhoads. Design and implementation of a tunable, Duffing-like electronic resonator via nonlinear feedback. *Journal of Microelectromechanical Systems*, 25(1):2–10, 2016.

[17] G. Arndt, E. Colinet, J. Arcamone, and J. Juillard. A design methodology for fully integrated MEMS and NEMS Pierce oscillators. *Sensors and Actuators A: Physical*, 172(1):293 – 300, 2011.

[18] J. T. M. van Beek and R. Puers. A review of MEMS oscillators for frequency reference and timing applications. *Journal of Micromechanics and Microengineering*, 22(1):013001, 2012.

[19] D. Psychogiou, R. Goamez-Garcia, and D. Peroulis. Acoustic wave resonator-based absorptive bandstop filters with ultra-narrow bandwidth. *IEEE Microwave and Wireless Components Letters*, 25(9):570–572, 2015.

[20] H. Yagubizade, M. Darvishi, M. C. Elwenspoek, and N. R. Tas. A 4th-order band-pass filter using differential readout of two in-phase actuated contour-mode resonators. *Applied Physics Letters*, 103(17):173517, 2013.

[21] A. B. Sabater, V. Kumar, A. Mahmood, and J. F. Rhoads. On the nonlinear dynamics of electromagnetically transduced microresonators. *Journal of Microelectromechanical Systems*, 22(5):1020–1031, 2013.

[22] L. Yu, H. Pajouhi, M. R. Nelis, J. F. Rhoads, and S. Mohammadi. Tunable, dual-gate, silicon-on-insulator (SOI) nanoelectromechanical resonators. *IEEE Transactions on Nanotechnology*, 11(6):1093–1099, 2012.

[23] P. Horowitz and W. Hill. *The Art of Electronics*. Cambridge University Press, New York, NY, USA, 2015.